

***In vivo* fluorescence imaging of primate retinal ganglion cells and retinal pigment epithelial cells**

Daniel C. Gray^{1,2}, William Merigan^{1,3}, Jessica I. Wolfing^{1,2}, Bernard P. Gee¹, Jason Porter¹, Alfredo Dubra¹, Ted H. Twietmeyer¹, and Kamran Ahmad¹

Center for Visual Science, University of Rochester, Rochester, NY, 14627¹

Institute of Optics, University of Rochester, Rochester, NY, 14627²

University of Rochester Eye Institute, Rochester, NY, 14642³

dgray@cvs.rochester.edu

Remy Tumar

Department of Molecular Biology and Genetics, Cornell University, Ithaca, NY, 14853

Fred Reinholz

Lasers and Bioengineering Group, Lions Eye Institute, Nedlands, WA 6009, Perth, Australia

David R. Williams^{1,2}

Center for Visual Science, University of Rochester, Rochester, NY, 14627¹

Institute of Optics, University of Rochester, Rochester, NY, 14627²

Abstract: The ability to resolve single cells noninvasively in the living retina has important applications for the study of normal retina, diseased retina, and the efficacy of therapies for retinal disease. We describe a new instrument for high-resolution, *in vivo* imaging of the mammalian retina that combines the benefits of confocal detection, adaptive optics, multispectral, and fluorescence imaging. The instrument is capable of imaging single ganglion cells and their axons through retrograde transport in ganglion cells of fluorescent dyes injected into the monkey lateral geniculate nucleus (LGN). In addition, we demonstrate a method involving simultaneous imaging in two spectral bands that allows the integration of very weak signals across many frames despite inter-frame movement of the eye. With this method, we are also able to resolve the smallest retinal capillaries in fluorescein angiography and the mosaic of retinal pigment epithelium (RPE) cells with lipofuscin autofluorescence.

©2006 Optical Society of America

OCIS codes: (330.4460) Ophthalmic optics; (010.1080) Adaptive optics; (170.3010) Image reconstruction techniques

References and Links

1. W. Drexler, U. Morgner, R. K. Ghanta, F. X. Kartner, J. S. Schuman and J. G. Fujimoto, "Ultra-high-resolution ophthalmic optical coherence tomography," *Nat. Med* **7**, 502-507 (2001).
2. R. a. Leitgeb, W. Drexler, A. Unterhuber, B. Hermann, T. Bajraszewski, T. Le, A. Stingl and A. F. Fercher, "Ultra-high resolution Fourier domain optical coherence tomography," *Opt. Express* **12**, 2156-2165 (2004).
3. B. Cense and N. A. Nassif, "Ultra-high-resolution high-speed retinal imaging using spectral-domain optical coherence tomography," *Opt. Express* **12**, 2435-2447 (2004).
4. M. Wojtkowski, V. J. Srinivasan, T. H. Ko, J. G. Fujimoto, A. Kowalczyk and J. S. Duker, "Ultra-high-resolution, high-speed, Fourier domain optical coherence tomography and methods for dispersion compensation," *Opt. Express* **12**, 2404-2422 (2004).
5. P. Artal and R. Navarro, "High-resolution imaging of the living human fovea: measurement of the intercenter cone distance by speckle interferometry," *Opt. Lett.* **14**, 1098-1100 (1989).

6. D. T. Miller, D. R. Williams, G. M. Morris and J. Liang, "Images of Cone Photoreceptors in the Living Human Eye," *Invest. Ophthalmol. Visual Sci.* **36**, S188-S188 (1995).
7. J. Liang and D. R. Williams, "Aberrations and retinal image quality of the normal human eye," *J. Opt. Soc. Am. A* **14**, 2873-2883 (1997).
8. J. Liang, D. R. Williams and D. Miller, "Supernormal vision and high-resolution retinal imaging through adaptive optics," *J. Opt. Soc. Am. A* **14**, 2884-2892 (1997).
9. F. Vargas-Martin, P. M. Prieto and P. Artal, "Correction of the aberrations in the human eye with a liquid-crystal spatial light modulator: limits to performance," *J. Opt. Soc. Am. A* **15**, 2552-2562 (1998).
10. A. Roorda and D. R. Williams, "The arrangement of the three cone classes in the living human eye," *Nature* **397**, 520-522 (1999).
11. G. Yoon, H. Hofer, L. Chen, B. Singer, J. Porter, Y. Yamauchi, N. Doble and D. R. Williams, "Dynamic correction of the eye's aberration with the Rochester 2nd generation adaptive optics system.," *Invest. Ophthalmol. Visual Sci.* **42**, S99-S99 (2001).
12. H. Hofer, L. Chen, G. Y. Yoon, B. Singer, Y. Yamauchi and D. R. Williams, "Improvement in retinal image quality with dynamic correction of the eye's aberrations," *J. Opt. Soc. Am. A* **8**, 631-643 (2001).
13. A. Roorda, A. B. Metha, P. Lennie and D. R. Williams, "Packing arrangement of the three cone classes in primate retina," *Vision Res.* **41**, 1291-1306 (2001).
14. A. Roorda and D. R. Williams, "Optical fiber properties of individual human cones," *J. Vis.* **2**, 404-412 (2002).
15. A. Roorda, F. Romero-Borja, W. J. Donnelly, H. Queener, T. J. Hebert and M. C. W. Campbell, "Adaptive optics scanning laser ophthalmoscopy," *Opt. Express* **10**, 405-412 (2002).
16. A. Pallikaris, D. R. Williams and H. Hofer, "The Reflectance of Single Cones in the Living Human Eye," *Invest. Ophthalmol. Vis. Sci.* **44**, 4580-4492 (2003).
17. J. Carroll, M. Neitz, H. Hofer, J. Neitz and D. R. Williams, "Functional photoreceptor loss revealed with adaptive optics: An alternate cause of color blindness," *Proc. Natl. Acad. Sci. U.S.A.* **101**, 8461-8466 (2004).
18. M. Glanc, E. Gendron, F. Lacombe, D. Lafaille, J. F. Le Gargasson and P. Lena, "Towards wide-field retinal imaging with adaptive optics," *Opt. Commun.* **230**, 225-238 (2004).
19. N. M. Putnam, H. J. Hofer, N. Doble, L. Chen, J. Carroll and D. R. Williams, "The locus of fixation and the foveal cone mosaic," *J. Vis.* **5**, 632-639 (2005).
20. W. Jiang, N. Ling, Y. Zhang, Y. Zeping, R. Xuejun, C. Gaun, C. Wang, L. Xue and E. Li, "Medical and Industrial Application of Adaptive Optics in Institute of Optics and Electronics, Chinese Academy of Sciences," in 5th International Workshop on Adaptive Optics for Industry and Medicine, (2005)
21. H. Hofer, J. Carroll, J. Neitz, M. Neitz and D. R. Williams, "Organization of the human trichromatic cone mosaic," *J. Neurosci.* **26**, 722-722 (2006).
22. D. X. Hammer, R. D. Ferguson, C. E. Bigelow, N. V. Ifimia and T. E. Ustun, "Adaptive optics scanning laser ophthalmoscope for stabilized retinal imaging," *Opt. Express* **14**, 3354-3367 (2006).
23. D. Merino, C. Dainty, A. Bradu and A. G. Podoleanu, "Adaptive optics enhanced simultaneous en-face optical coherence tomography and scanning laser ophthalmoscopy," *Opt. Express* **14**, 3345-3353 (2006).
24. J. I. Wolfing, M. Chung, J. Carroll, A. Roorda and D. R. Williams, "High-resolution retinal imaging of cone-rod dystrophy," *Ophthalmology* **113**, 1014-1019 (2006).
25. A. Bindewald, J. J. Jorzik, A. Loesch, F. Schutt and F. G. Holz, "Visualization of retinal pigment epithelial cells in vivo using digital high-resolution confocal scanning laser ophthalmoscopy," *Am. J. Ophthalmol.* **137**, 556-558 (2004).
26. M. F. Cordeiro, L. Guo, V. Luong, G. Harding, W. Wang, H. E. Jones, S. E. Moss, A. M. Sillito and F. W. Fitzke, "Real-time imaging of single nerve cell apoptosis in retinal neurodegeneration," *Proc. Natl. Acad. Sci. U.S.A.* **101**, 13352-13356 (2004).
27. Y. Imanishi, D. W. Piston, W. Baehr, and K. Palczewski, "Noninvasive two-photon imaging reveals retinyl ester storage structures in the eye," *J. Cell. Biol.* **164**, 373-383 (2004).
28. B. Hermann, E. J. Fernandez, A. Unterhuber, H. Sattmann, A. F. Fercher, W. Drexler, P. M. Prieto and P. Artal, "Adaptive-optics ultrahigh-resolution optical coherence tomography," *Opt. Lett.* **29**, 2142-2144 (2004).
29. Y. Zhang, J. T. Rha, R. S. Jonnal and D. T. Miller, "Adaptive optics parallel spectral domain optical coherence tomography for imaging the living retina," *Opt. Express* **13**, 4792-4811 (2005).
30. E. J. Fernandez, B. Povazay, B. Hermann, A. Unterhuber, H. Sattmann, P. M. Prieto, R. Leitgeb, P. Ahnelt, P. Artal and W. Drexler, "Three-dimensional adaptive optics ultrahigh-resolution optical coherence tomography using a liquid crystal spatial light modulator," *Vision Res.* **45**, 3432-3444 (2005).
31. R. J. Zawadzki, S. M. Jones, S. S. Olivier, M. T. Zhao, B. A. Bower, J. A. Izatt, S. Choi, S. Laut and J. S. Werner, "Adaptive-optics optical coherence tomography for high-resolution and high-speed 3D retinal in vivo imaging," *Opt. Express* **13**, 8532-8546 (2005).
32. D. T. Miller, Associate Professor of Optometry, Indian University School of Optometry, 800 E. Atwater Ave, Bloomington, IN 47405 (Personal Communication, 2006).
33. D. M. Dacey, B. B. Peterson, F. R. Robinson, P. D. Gamlin, "Fireworks in the primate retina: In vitro photodynamics reveals diverse LGN-projecting ganglion cell types," *Neuron* **37**, 15-27 (2003).
34. O. Strauss, "The retinal pigment epithelium in visual function," *Physiol. Rev.* **85**, 845-881 (2005).

35. L. Feeney-Burns, E. S. Hilderbrand and S. Eldridge, "Aging Human Rpe - Morphometric Analysis of Macular, Equatorial, and Peripheral Cells," *Invest. Ophthalmol. Vis. Sci.* **25**, 195-200 (1984).
36. K. M. Zinn and J. V. Benjamin-Henkind, "Anatomy of the human retinal pigment epithelium", in *The Retinal Pigment Epithelium*, K. M. Zinn and M. F. Marmor (Harvard University Press, Cambridge, 1979).
37. D. M. Snodderly, M. M. Sandstrom, I. Y. F. Leung, C. I. Zucker and M. Neuringer, "Retinal pigment epithelial cell distribution in central retina of rhesus monkeys," *Invest. Ophthalmol. Visual Sci.* **43**, 2815-2818 (2002).
38. C. A. Curcio, K. R. Sloan, R. E. Kalina and A. E. Hendrickson, "Human Photoreceptor Topography," *J. Comp. Neurol.* **292**, 497-523 (1990).
39. F. C. Delori, "Spectrophotometer for noninvasive measurement of intrinsic fluorescence and reflectance of the ocular fundus.," *Appl. Opt.* **33**, 7439-7452 (1994).
40. F. C. Delori, C. K. Dorey, G. Staurenghi, O. Arend, D. G. Goger and J. J. Weiter, "In vivo fluorescence of the ocular fundus exhibits retinal pigment epithelium lipofuscin characteristics," *Invest. Ophthalmol. Visual Sci.* **36**, 718-729 (1995).
41. A. von Ruckmann, F. W. Fitzke and A. C. Bird, "Distribution of fundus autofluorescence with a scanning laser ophthalmoscope," *Br. J. Ophthalmol.* **79**, 407-412 (1995).
42. N. Lois, A. S. Halfyard, A. C. Bird and F. W. Fitzke, "Quantitative evaluation of fundus autofluorescence imaged "in vivo" in eyes with retinal disease," *Br. J. Ophthalmol.* **84**, 741-745 (2000).
43. F. G. Holz, C. Bellman, S. Staudt, F. Schutt and H. E. Volcker, "Fundus autofluorescence and development of geographic atrophy in age-related macular degeneration," *Invest. Ophthalmol. Visual Sci.* **42**, 1051-1056 (2001).
44. F. C. Delori, D. G. Goger and C. K. Dorey, "Age-related accumulation and spatial distribution of lipofuscin in RPE of normal subjects," *Invest. Ophthalmol. Visual Sci.* **42**, 1855-1866 (2001).
45. N. Lois, A. S. Halfyard, A. C. Bird, G. E. Holder and F. W. Fitzke, "Fundus autofluorescence in Stargardt macular dystrophy-fundus flavimaculatus," *Am. J. Ophthalmol.* **138**, 55-63 (2004).
46. F. Reinholz, R. A. Ashman and R. H. Eikelboom, "Simultaneous three wavelength imaging with a scanning laser ophthalmoscope," *Cytometry* **37**, 165-170 (1999).
47. ANSI, *American National Standard for the Safe Use of Lasers ANSI Z136.1-2000*, (Laser Institute of America, Orlando, FL 2000).
48. H. Hofer, P. Artal, B. Singer, J. L. Aragon and D. R. Williams, "Dynamics of the eye's wave aberration," *J. Opt. Soc. Am. A* **18**, 497-506 (2001).
49. J. Cushion, F. N. Reinholz and B. A. Patterson, "General purpose control system for scanning laser ophthalmoscopes," *Clin Experiment Ophthalmol* **31**, 241-245 (2003).
50. P. M. Bischoff, H. J. Niederberger, B. Torok and P. Speiser, "Simultaneous Indocyanine Green and Fluorescein Angiography," *Retina* **15**, 91-99 (1995).
51. A. F. Fuchs and R. A. Robinson, "A method for measuring horizontal and vertical eye movement chronically in the monkey," *J. Appl. Physiol.* **21**, 1068-1070 (1966).
52. N. J. Coletta and D. R. Williams, "Psychophysical Estimate of Parafoveal Cone Spacing," *J. Opt. Soc. Am. A Opt. Image Sci. Vis.* **3**, P92-P93 (1986).
53. G. Wyszecki and W. S. Stiles, *Color Science: Concepts and Methods, Quantitative Data and Formulas* (John Wiley & Sons, Inc., New York, 1982), Chap. 2.
54. J. M. Burke and L. M. Hjelmeland, "Mosaicism of the retinal pigment epithelium: seeing the small picture," *Mol. Interv.* **5**, 241-249 (2005).
55. O. Packer, a. E. Hendrickson and C. a. Curcio, "Photoreceptor Topography of the Retina in the Adult Pigtail Macaque (*Macaca Nemestrina*)," *J. Comp. Neurol.* **288**, 165-183 (1989).
56. R. S. Weinhaus, J. M. Burke, F. C. Delori and D. M. Snodderly, "Comparison of Fluorescein Angiography with Microvascular Anatomy of Macaque Retinas," *Exp. Eye Res.* **61**, 1-16 (1995).

1. Introduction

Optical imaging has long been a preferred method to noninvasively investigate the normal retina, the diseased retina, and the efficacy of retinal therapy. Until recently, the resolution at which images could be recovered from the retina *in vivo* has been limited to a macroscopic spatial scale. Optical coherence tomography now can provide an axial resolution that is 2-3 μm [1-4], clearly revealing the individual layers of the retina. Artal and Navarro [5] showed, using a method similar to speckle interferometry, that quantitative information about the cone mosaic can be obtained *in vivo*, and Miller et al. [6] demonstrated that cone photoreceptors can be directly imaged in the living human eye. The introduction of adaptive optics ophthalmoscopes has improved the transverse resolution to less than 2 μm so that single cells, especially cones, can be routinely resolved [7-24]. Cones have proven particularly accessible to *in vivo* cellular imaging because their waveguide properties cause them to return light

preferentially back through the eye's pupil [14]. Recently, there have been reports of *in vivo* imaging of other cell types in the retina [15,25-27]. The application of adaptive optics to optical coherence tomography (AO OCT) [23,28-31] has demonstrated extremely fine axial and transverse resolution *in vivo*, but so far it has not generated images of single retinal cells that have not been resolved by other means.

Retinal ganglion cells are of interest because they provide the retinal output signal to the brain, the functional role is unknown for most of the 15-20 morphologically distinct ganglion cell classes, and they are one of the most vulnerable retinal cells to eye disease. Ganglion cell loss is the cause of blindness in glaucoma, the most prevalent cause of irreversible blindness in the United States. However, ganglion cells are difficult to image because their reflectance is roughly 60 times less than that of cones [32] and they are entangled with Müller and amacrine cells of similar refractive index. Fluorescence imaging with the use of dyes or natural fluorophores is a means of providing contrast to transparent retinal cells that has rarely been applied to *in vivo* high-resolution retinal imaging. *In vitro* imaging of ganglion cells was demonstrated by using retrograde labeling techniques through injections into the lateral geniculate nucleus (LGN) region of primate brain by Dacey et al. [33]. Also, Cordeiro et al. [26] showed that ganglion cells undergoing experimentally induced cell death in rats and primates can be individually imaged in real time *in vivo* by intravitreal injections of an Annexin 5-bound fluorophore. Here, we capitalize on the use of rhodamine and Alexa fluorescent markers injected into the LGN to label single ganglion cells in the retina *in vivo*, and image them with an adaptive optics scanning laser ophthalmoscope.

RPE cells are responsible for assisting in the regeneration of retinal in the visual cycle, for providing the metabolic support needed by the photoreceptors, and for the phagocytosis of the photoreceptor outer segments [34]. Additionally, RPE cells are affected in retinal diseases including age-related macular degeneration, Stargardt's macular dystrophy, and Best's disease [34]. Despite their important role in the retina, RPE cell morphology across retinal eccentricity has not been studied to the same extent as the structure of the photoreceptors, though some reports of cell size and density as a function of eccentricity are available [35-38]. RPE cells are not usually resolved in conventional scanning laser ophthalmoscopes, even those that are equipped with adaptive optics, presumably because they are obscured by the waveguiding photoreceptors that lie immediately in front of them in the retina. Several *in vivo* techniques have been developed showing the distribution of lipofuscin autofluorescence across the normal and diseased retina [25,39-45]. Imansishi et. al. [27] acquired *in vivo* images of mouse RPE cells with two-photon microscopy by imaging through the sclera. To our knowledge, individual primate RPE cells have not been resolved at high resolution *in vivo*. One of the difficulties in imaging RPE cells *in vivo* in the human is that autofluorescence images are blurred by eye motion during the long integration times required given the weak autofluorescence signal. Here, we combine a method involving simultaneous imaging in two spectral bands that allows the integration of very weak signals across many frames despite inter-frame eye movements. With this method, we are able to resolve the mosaic of RPE cells using lipofuscin autofluorescence.

2. Methods

2.1 The Fluorescence AOSLO Instrument

The fluorescence adaptive optics scanning laser ophthalmoscope (AOSLO) shown in Fig. 1 consists of an adjustable scanning system with a variable 1- to 3.5-degree field of view, an adaptive optics system (consisting of a Shack-Hartmann wavefront sensor, a MEMS deformable mirror, and a laser beacon), two imaging lasers, and two detectors for simultaneous reflectance and fluorescence imaging. Two computer systems are employed, one for controlling the AO correction and another for acquiring retinal images. The fluorescence AOSLO design was adapted from the first AOSLO demonstrated by Austin

Roorda and colleagues in 2002 [15] and from a simultaneous three-wavelength scanning laser ophthalmoscope demonstrated by Reinholz and colleagues [46].

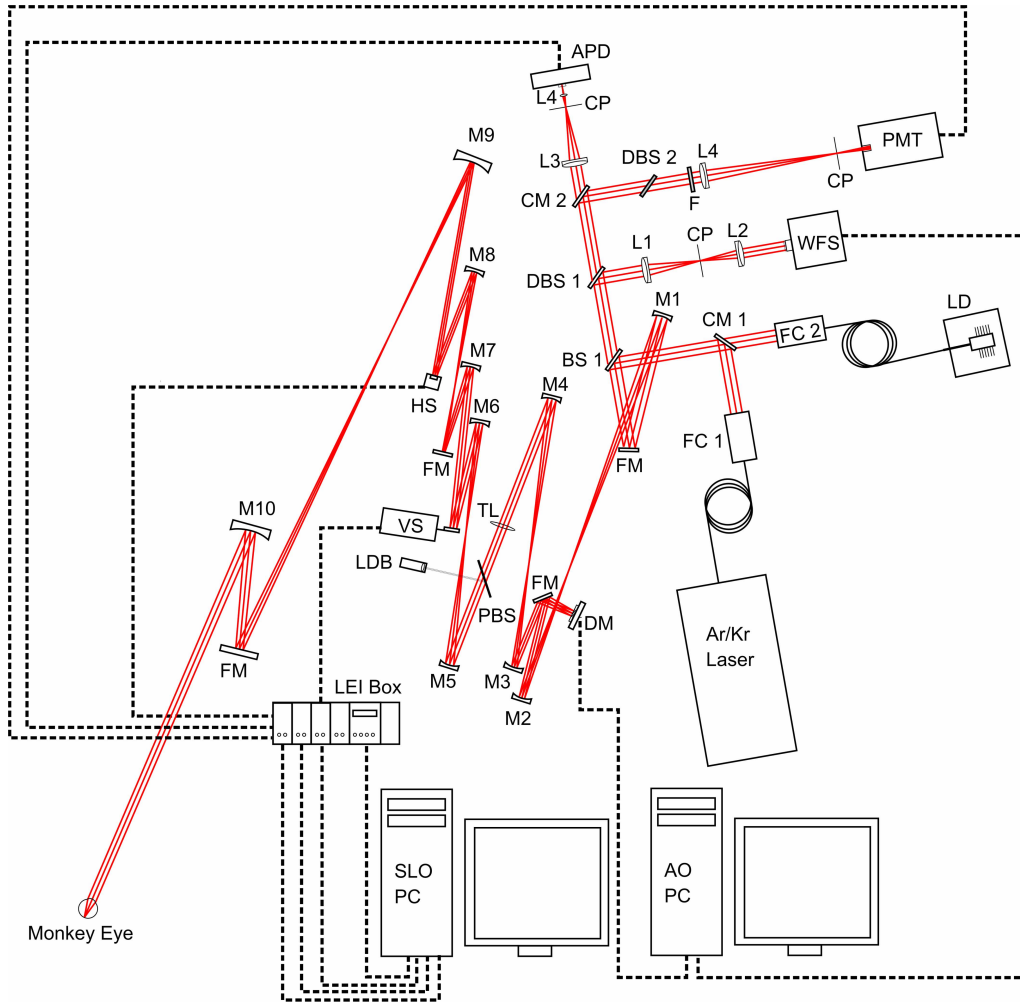


Fig. 1. The fluorescence Adaptive Optics Scanning Laser Ophthalmoscope. L: lenses, M: spherical mirrors, FM: fold mirrors, CM: cold mirrors, FC: fiber collimators, DBS: dichroic beam splitters, CP: confocal pinholes, LD: 830-nm fiber coupled laser diode, LDB: laser diode beacon, BS 1: 90/10 parallel plate AR coated beam splitter, DM: MEMS deformable mirror, TL: ophthalmic trial lens, PBS: pellicle beam splitter, VS: vertical scanner (26 Hz), HS: horizontal scanner (15.1 kHz), F: band pass fluorescence filter, PMT: photomultiplier tube, APD: avalanche photodiode, LEI Box: scanner control electronics.

2.2 Laser Sources

A single-mode fiber-coupled 830-nm laser diode (Axcel Photonics, Marlborough, MA USA) is used for reflectance imaging of the retina. Near infrared (NIR) wavelengths are optimal for reflectance imaging, because the ANSI guide for the safe use of lasers [47] are more relaxed and more light is reflected from the retina in this part of the spectrum. In addition, NIR wavelengths are near the peak quantum efficiency of the silicone avalanche photodiode (APD) used to capture the reflectance image.

An air-cooled argon/krypton laser (Melles Griot, Carlsbad, CA USA) with nine lines from 476 nm to 676 nm provides wavelengths for fluorescence excitation. The output of the laser is passed through a variable frequency acousto-optic modulator (AOM) (Brimrose, Baltimore, MD USA) for shutter control and light modulation. Light can be modulated pixel-by-pixel using a PCI pattern generator (Spectrum, Grosshansdorf, Germany), which is synchronized to the scanning system. Output light from the AOM is coupled into a single mode, polarization-maintaining optical fiber for delivery to the AOSLO system. A cold mirror (CM 1) permits both sources to enter the system simultaneously and pass through the same entrance pupil into the system, the image of which has a diameter of 6.6 mm at the pupil of the eye. A 90/10 anti-reflection (AR) coated parallel plate beam splitter (BS 1) oriented at 45 degrees reflects imaging light into the system and transmits light for wavefront sensing and retinal imaging. A 904-nm, 30-mW laser diode (LDB) is used as a beacon for the adaptive optics system. The collimated laser beam diameter is 1.5 mm at the eye's pupil, which produces a diffraction-limited spot on the retina with a large depth of focus, which is suitable for wavefront sensing. The beacon is inserted into the system with a pellicle beam splitter (PBS) after the deformable mirror (DM) to avoid back scatter from the DM surface, but before the scanners to avoid coherent speckle effects [48]. Scanning reduces speckle by averaging the wavefront measurement over the entire field of view, yielding a more uniform wavefront correction [15,48].

2.3 Optical Path

The optical path consists of four pupil planes (residing at the MEMS DM, the intermediate trial lens plane, the vertical scanner, and the horizontal scanner) imaged to the eye's pupil by a series of off-axis spherical mirror telescopes. Zemax design software (Bellevue, WA USA) was used to optimize the angles and surface placements to minimize the system aberrations. Most of the astigmatism in the system, due to using spherical mirrors off-axis, is corrected with a cylindrical ophthalmic trial lens placed at the intermediate trial lens plane (TL). Also, this conjugate pupil plane provides a convenient location to correct the eye's lower order aberrations - defocus and astigmatism - with standard ophthalmic trial lenses.

The horizontal scanner (HS) is a high frequency resonant scanner (Electro-Optical Products Corp, Glendale, NY USA), and is driven sinusoidally at 15.1 kHz. The sinusoidal scan results in image warp in the horizontal direction due to the constantly changing velocity of the horizontal scanner. To remove the warp from the images, we first measure the horizontal warp with a linear line-pair grating placed at the focal plane of a model eye lens inserted at the eye's pupil plane. Using a custom Matlab (Mathworks, Natick, MA USA) based algorithm, the retinal image is stretched and compressed in the appropriate manner to reverse the effect of the scan warp [15]. A slow galvanometric scanner (VS) (GSI Lumonics, Bedford, MA USA) is coupled to the horizontal scanner and is driven in a saw-tooth pattern at 26 Hz to give the vertical scan. By adjusting both scanner amplitudes electronically, the imaging field of view can be adjusted from 1 to 3.5 degrees.

2.4 Adaptive Optics

The adaptive optics system consists of a MEMS deformable mirror (DM) and a Shack-Hartman wavefront sensor (WFS). Conjugate with the pupil plane of the eye, the WFS consists of a lenslet array (Adaptive Optics Associates, Cambridge, MA USA) with 18 mm focal length lenslets spaced at 328 μm , and a digital camera (Cohu, San Diego, CA USA). The camera captures frames at 30 Hz and the wavefront aberration is computed at 12 Hz for a 1004 x 1004 pixel array. Ninety-five percent of the light from the 904-nm laser diode is directed to the WFS by a 45-degree dichroic beam splitter (DBS 1). The beam splitter passes wavelengths less than 830 nm to the imaging detectors. The MEMS DM (Boston Micromachines Corporation, Boston, MA USA) is a 4- μm stroke continuous membrane mirror with 144 electrostatic actuators arranged in a square array (12 x 12). The actuator

spacing is 400 μm , resulting in a 4.8-mm diameter aperture. The mirror is driven by a high voltage power supply that pulls down the membrane mirror surface under each actuator with applied voltage. The AO control drives the DM using a least squares inverse of the response matrix of the system [12].

2.5 Light Detection

Light for detection is split by a cold mirror (CM 2) which passes the 830 nm light for reflectance imaging to the avalanche photodiode (APD) (Perkin Elmer, Vaudreuil, QC Canada), with a custom built amplifier and power supply designed and built at the Center for Visual Science and the visible light to the photomultiplier tube (PMT) (Hamamatsu, Shizuoka-ken, Japan). The PMT housing includes an electronic shutter (Melles Griot, Rochester, NY USA) to prevent damage from excess light. Appropriate dichroic mirrors and filters are placed in front of the PMT for fluorescence imaging. Both detectors have removable confocal pinholes (CP) placed at retinal conjugate planes.

2.6 Electronic Hardware

The SLO system timing is dictated by the synchronization signal generated by the horizontal scanner. This signal is input to specialized control hardware (LEI box) from the Lions Eye Institute [49] (LEI, Perth Australia) that uses the horizontal scanner signal to create a voltage ramp for stepping the vertical scanner. It also generates the *hsync* and *vsync* signals for recreating the image in a frame grabber on the SLO PC.

The current signals from the APD and PMT are converted to voltages through custom-built and off-the-shelf transimpedance amplifiers (Femto, Berlin, Germany). These signals are then connected to a custom-built, three-channel video signal conditioning board. This board provides up to 40x gain per channel and adds in a computer adjustable blanking period to the incoming signal. Corresponding APD and PMT outputs from the video board are connected to a 4-channel frame grabber (Matrox, Dorval, QC Canada). The *hsync* and *vsync* signals from the LEI hardware are used by the frame grabber to generate a 512 x 512 pixel digital image from the incoming video signal at a 26-Hz frame rate.

2.7 Simultaneous image capture and dual registration

The low light levels from *in vivo* fluorescence imaging require that hundreds of frames be averaged to increase the signal-to-noise ratio. Inter-frame eye movements due to the monkey's cardiac rhythm preclude averaging many fluorescence frames together. When ganglion cells were strongly labeled, each fluorescence frame contained enough spatial structure to cross-correlate. However, with weakly labeled ganglion cells and RPE cells, each fluorescence frame did not contain adequate spatial structure to cross-correlate. Other groups have used multiple detectors to acquire images of the retina in different spectral bands simultaneously [46,50]. We combat the problem of low signal by simultaneously capturing reflectance and fluorescence images using the APD and PMT detectors, respectively. Each reflectance frame has high enough signal to successfully estimate the image motion using a normalized cross-correlation. We have developed a dual registration technique where the image motions are calculated and the appropriate shifts are applied to both the reflectance and fluorescence images. The frames are averaged to produce the final registered reflectance and fluorescence retinal images. The total processing time for one image varied from five to 60 minutes depending on number of frames, size of cross-correlation areas, and the speed of the processing computer. The number of frames used to create each image is labeled in the figure captions.

2.8 Ganglion cell labeling and imaging

To image ganglion cells *in vivo* we injected fluorescent dye into the right lateral geniculate nucleus (LGN) of a healthy adult macaque nemestrina monkey. Small injections (200 nl to

800 nl) were made under physiological guidance into selected locations in the LGN so that numerous experiments could be done in the same monkey. The LGN was first mapped using tungsten electrodes and then injections were precisely positioned using a recording/injecting microelectrode while the awake monkey maintained fixation. Imaging started after at least five to six days post-injection to allow retrograde transport of the dye along retinal ganglion cell axons and into the soma of ganglion cells [33]. For physiological recording, a chronic scleral search coil and head restraint system [51] were implanted in the monkey under general anesthesia using aseptic surgical methods. A chronic recording chamber (Crist Instruments, Hagerstown, MD USA) was also implanted at a location that permitted access to the LGN and other thalamic visual nuclei. Individual injections used either rhodamine dextran or Alexa 594 conjugated to dextran. Rhodamine dye was excited with 530 nm light and imaged with a 555-nm dichroic and 40-nm bandwidth filter centered at 593 nm, while Alexa 594 dye was excited at 568 nm and imaged with a 583-nm dichroic and a 40-nm bandwidth filter centered at 624 nm. All experimental protocols were approved by the University Committee of Animal Resources at the University of Rochester Medical Center and complied with the Public Health Service policy on Humane Care and Use of Laboratory Animals.

2.9 RPE cell imaging

Autofluorescence images were taken by exciting lipofuscin, the intrinsic fluorophore contained in the RPE cell cytoplasm, with 568 nm light, and the fluorescence was imaged with a 583-nm dichroic and a 40-nm bandwidth filter centered at 624 nm. Lipofuscin has a broad excitation range with a peak at 514 nm [40]. The images in this paper were taken by exciting at 568 nm, however we have also obtained images with an excitation wavelength of 530 nm. For our imaging conditions, the ANSI guide for the safe use of lasers [47] allow 4.5 times greater exposure to 568 nm light than 530 nm light; because of this it was advantageous to excite lipofuscin with the longer wavelength light.

2.10 RPE cell mosaic analysis

From the registered RPE images, x-y coordinates of each RPE cell were manually selected (NIH ImageJ). A radial average of the two-dimensional Fourier transform of the RPE cell mosaic was computed. The peak of the annulus of the radial average was defined as the modal cell spacing in the frequency domain [52]. Cell density estimates correspond to the ratio of cells divided by the area in which the cells were visible (e.g. where they were not obscured by the retinal vasculature).

2.11 Power levels

Images were taken with simultaneous exposure of light at three wavelengths: 530 nm or 568 nm for fluorescence excitation, 830 nm light for reflectance imaging, and 904 nm light for wavefront measurement. The combined photochemical and thermal exposure was kept below the maximum permissible exposure limit (MPE) as stated in the ANSI guide for the safe use of lasers [47] for extended sources for a two-hour exposure time. To image rhodamine dextran dye without adaptive optics, the retina was simultaneously exposed to 120 μ W at 530 nm, 436 μ W at 830 nm for a 2-degree imaging field. To image lipofuscin containing RPE cells and alexa 594 labeled ganglion cells with adaptive optics, the retina was simultaneously exposed to 256 μ W at 568 nm, 320 μ W at 830 nm and 57 μ W at 904 nm for a 2-degree imaging field. To image sodium fluorescein without adaptive optics, a 15-minute exposure time was used and the retina was exposed to 55 μ W at 488 nm and 436 μ W at 830 nm for a 3.5-degree imaging field.

2.12 Monkey preparation

Retinal imaging was initiated about five days after dye injection and continued over the following five months. During imaging, the monkey was anesthetized with isoflurane (1-3 percent), pupils were dilated with one to two drops of cyclopentolate (10 percent), a lid speculum held the imaged eye open, and a rigid gas permeable contact lens, lubricated with a commercial wetting solution, was used to protect the cornea. The chronic head restraint system was used to align the monkey's eye with the imaging system. This was accomplished by connecting the head post to a goniometer and rotation mount centered on the nodal point of the eye that allowed the retinal imaging location to be shifted with minimal misalignment of the eye's pupil. A motorized three-axis translation stage (Velmex, Bloomfield, NY USA) was used to align the eye to the pupil plane of the AOSLO.

2.13 Angular and spatial retinal dimensions

To convert angular measures of the dimensions of imaged retinal structures to physical size, we assumed that the monkey retina had the same optical properties as the Le Grand model eye for the human [53], except that all dimensions were rescaled linearly to account for the smaller axial length of the monkey eye. The monkey eye had an axial length of 21.97 mm measured using an IOLMaster (Carl Zeiss Meditec, Jena, Germany), compared with 24.2 mm for the LeGrand model human eye. The retinal spatial-angular conversion was correspondingly reduced from 291 $\mu\text{m}/\text{deg}$ for the human to 264 $\mu\text{m}/\text{deg}$ for the particular monkey we imaged.

3. Results

All images were taken on the left eye of the macaque monkey whose lower order correction of defocus and astigmatism resulted in an average root means square (RMS) wavefront error of 0.2 to 0.3 μm over a 5.55-mm pupil as measured by our wavefront sensor. AO correction was performed over a 5.55-mm pupil with typical residual RMS wavefront error of 0.05 μm to 0.12 μm .

3.1 Ganglion cells

Excellent dye labeling of retinal ganglion cells was achieved after injections targeted to either the upper (P) or lower (M) layers of the LGN. Figure 2 shows ganglion cell bodies and axons labeled with either rhodamine dextran or Alexa 594 dyes from different regions of the retina. Figure 2 (a) was taken at an eccentricity of approximately 17 degrees nasal and 5 degrees inferior, just below the optic disk and shows labeled axons extending up and to the right from some of the labeled cells. The contrast of the image was enhanced to make the axons more visible, causing cell bodies to appear saturated. Figure 2 (b) was taken on the vertical meridian of the retina approximately 10 degrees inferior from the fovea and shows dense labeling of ganglion cells in the left half of the image which project to the injected LGN. The unlabeled ganglion cells on the right side of the image project to the opposite LGN. Ganglion cells in both 2 (a) and 2 (b) were labeled with rhodamine dextran dye and the images were taken before the adaptive optics and dual registration techniques had been implemented. Figures 2 (c) and (d) show the persistence of the dye labeled cells with Alexa 594 dye. Figure 2 (c) was taken 37 days after the injection and (b) was taken 77 days later. The four ganglion cells marked by arrows can be seen in both images. We observed that after a particularly dense injection, label could be seen five months after the injection. Only Fig. 2 (d) was taken with the use of adaptive optics. Here the adaptive optics was used to focus through the ganglion cell layer to find the best plane of focus in steps of 0.1 diopters (D).

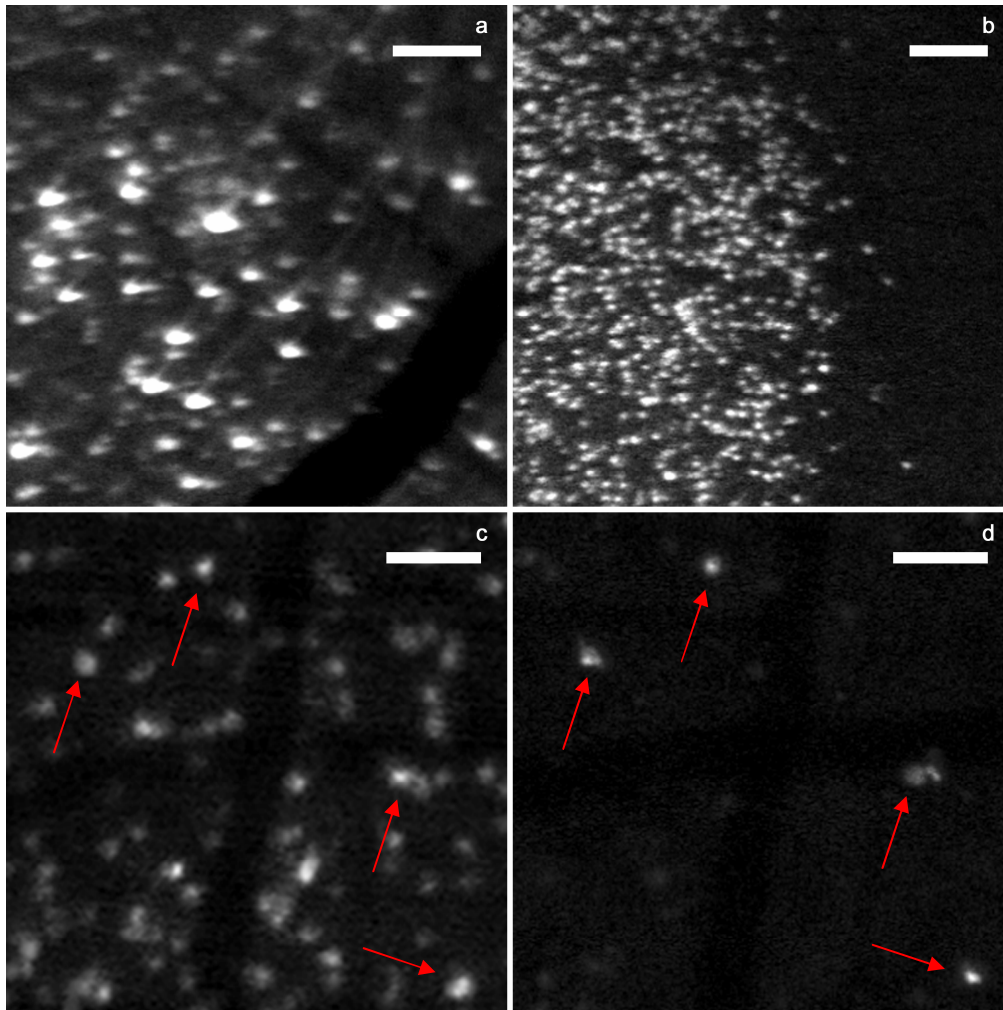


Fig. 2. (a) Ganglion cell bodies and axons labeled with rhodamine dextran dye. The image was taken at an eccentricity of approximately 17 degrees nasal and 5 degrees inferior, with the optic disk to the upper right of the image. (b) Ganglion cells labeled with rhodamine dextran dye at an eccentricity of approximately 10 degrees inferior along the vertical meridian. (c) Ganglion cells labeled with alexa 594 dye at an eccentricity of approximately 10 degrees infero-nasal, 37 days after labeling. (d) From the same location, taken 77 days after image (c) showing at least four ganglion cells that remained labeled. (a, b, c) taken without AO correction, (d) with closed loop AO correction, (a, b) taken without dual registration and (c, d) taken with dual registration. The images were constructed from (a) 500 frames, (b) 200 frames, (c) 512 frames, (d) 1000 frames. Scale bars: (a, b) 100 μm , (c, d) 50 μm .

3.2 *In vivo photodynamics*

Ganglion cells labeled with rhodamine dextran dye exhibited a brightening effect when the retinal light exposure was increased by three times. The effect was apparent while cells were being imaged, and the brightening could be enhanced by adjusting the scanner amplitudes to illuminate only a small 1-degree patch. Figure 3 shows the result of exposing one section of the retina to increased light for approximately 20 minutes. After exposure, shown in Fig. 3(b) the exposed cells were substantially brighter than cells that were not exposed. The extent of the exposure was larger than 1 degree due to eye motion.

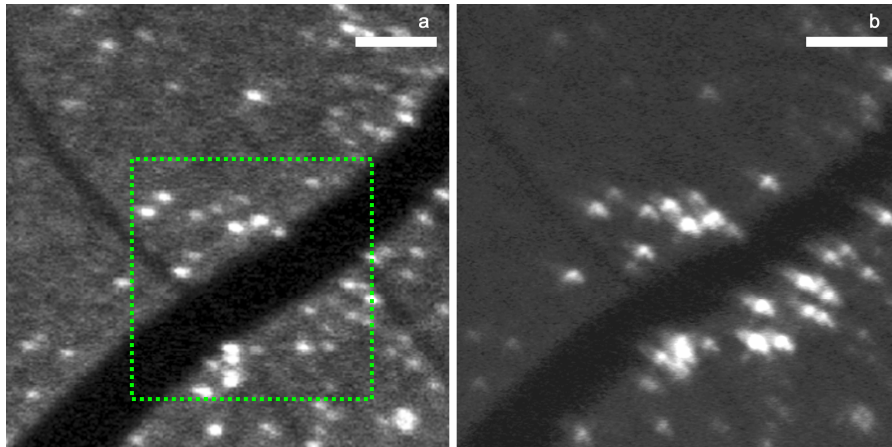


Fig. 3. (a) Located at an eccentricity of approximately 19 degrees nasal and 7 degrees inferior, ganglion cells labeled with rhodamine dextran dye. The image was taken before exposure to intense light, and cells were excited at 530 nm. The green box shows the approximate size of the exposed region (b). Increased intensity of cell fluorescence due to a 20-minute exposure of a 1-degree square area with 530-nm excitation. Both images were taken without adaptive optics or dual registration. 300 frames were used to create both images. Scale bars are 100 μm .

3.3 Retinal pigment epithelial cells

Individual RPE cells were imaged by exciting the lipofuscin fluorophores that are found naturally in RPE cell cytoplasm. Figure 4 (a) shows the RPE mosaic at approximately 10 degrees infero-nasal at the same location as the ganglion cells in Fig. 2 (c) and (d). Figure 4 (b) shows the RPE mosaic at the fovea. In both images the RPE cell mosaic appears in a honeycomb pattern, possibly because only the cytoplasm surrounding the nuclei of the cells contain fluorescent lipofuscin. Consistent with other reports, there was considerable variability in the amount of fluorescence observed in neighboring RPE cells [54]. Using the adaptive optics system, a through focus series in 0.1 D steps was taken through the retina to find the best plane of focus for the RPE cells. For both images, the dual registration technique described above was used.

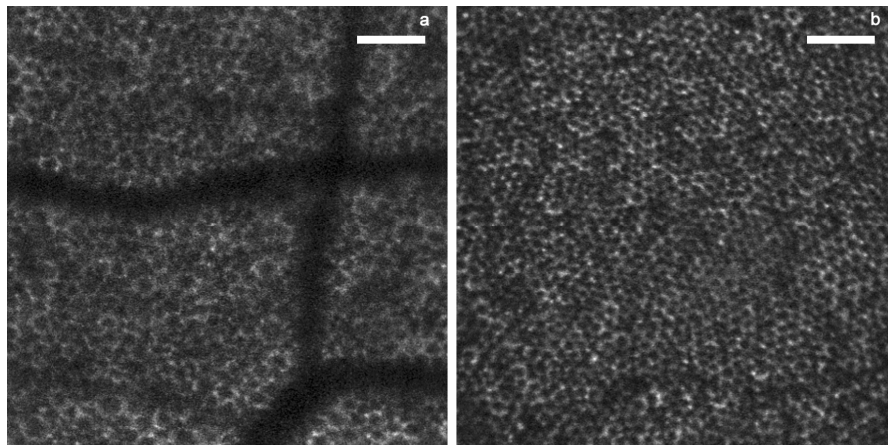


Fig. 4. RPE cells imaged at two retinal locations: (a) At an eccentricity of approximately 10 degrees infero-nasal at the same location as ganglion cells in Fig. 2 (c) and (d). (b) Centered at the fovea. Both images taken with the use of adaptive optics, dual registration, and were created with 1000 frames. Scale bars are 75 μm .

The RPE cells are roughly triangularly packed, most cells having six immediate neighbors. Figure 5 shows the radial power spectrum, where at 10 degrees eccentricity an annular peak of 15 cycles/degree was measured and correspondingly, 22.8 cycles/degree at the fovea. At 10 degrees eccentricity, the average modal cell spacing was 17.6 μm , while at the fovea the modal cell spacing was 11.6 μm . The cell density at 10 degrees eccentricity was found to be 2,876 cells/mm² and 6,339 cells/mm² at the fovea. Using methods described by Coletta and Willams [52], a perfect triangular spacing would yield modal spacing of 17.4 μm for the same density at 10 degrees and 11.7 μm at the fovea. In comparison, Snodderly et al. [37] measured the RPE density of eight rhesus monkeys, and reported an average of $3,997 \pm 551$ cells/mm² at 9 degrees eccentricity and $7,139 \pm 1193$ cells/mm² at the fovea. We made simultaneous measurements of RPE and cone density at 10 degrees eccentricity, where cone density was found to be 13,275 cells/mm², similar to previous measurements of cone density in three macaque nemestrina monkeys of 12,000 cones/mm² on average [55]. Our measured density of cones at 10 degrees eccentricity is 4.6 times greater than that of RPE cells, making RPE cells easily distinguishable from cones.

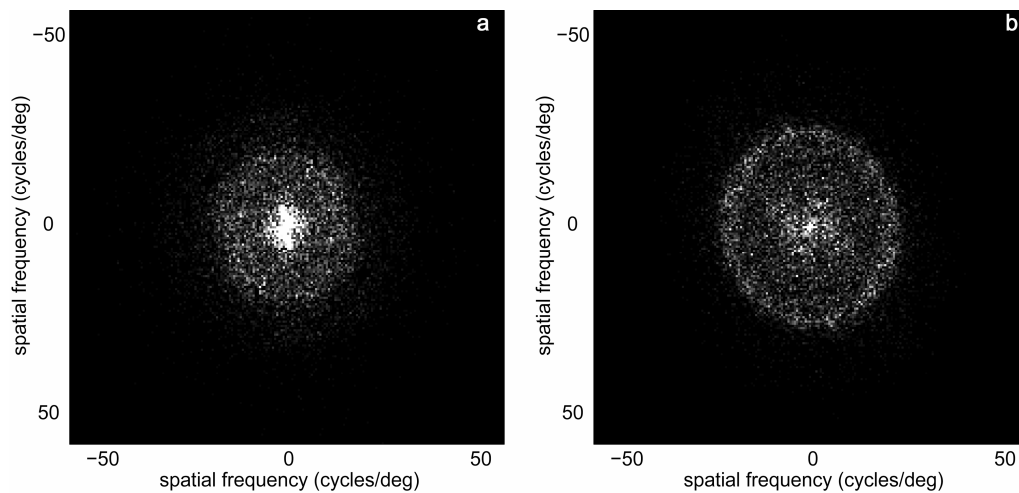


Fig. 5. (a) Two-dimensional power spectrum corresponding to the RPE mosaic in Fig. 4 (a).
 (b) Two-dimensional power spectrum corresponding to the RPE mosaic in Fig. 4 (b).

3.4 Fluorescein angiography of the foveal avascular zone

The macaque monkey was given a 0.7 ml intravenous injection of 10 percent sodium fluorescein dye. Using 488-nm excitation, a 495-nm long pass dichroic and 35-nm band pass filter centered at 520 nm, the complete capillary bed surrounding the avascular zone of the monkey was visible. The image was taken without the use of adaptive optics, and the best focus was achieved using trial lenses. (See linked (2 MB) movie file for real-time filling of the vasculature.)

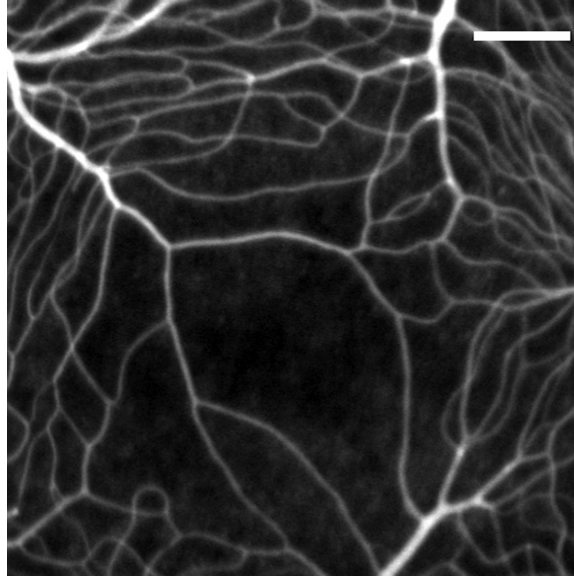


Fig. 6. Intravenous injection of sodium fluorescein dye centered at the fovea with a 3.5-degree field of view. The image was taken without adaptive optics, and 1918 fluorescence frames were dual registered. See linked (2 MB) movie file for real time filling of the vasculature. Scale bar is 150 μm .

4. Discussion

4.1 Ganglion cell imaging *in vivo*

To our knowledge, this is the first report of imaging healthy primate ganglion cells and their axons *in vivo*. Cordeiro et al. [26] have previously shown that ganglion cells undergoing experimentally induced cell death in rats and primates can be individually imaged in real time *in vivo* using intravitreal injections of Annexin 5-bound fluorophore. The technique used a prototype Zeiss confocal laser scanning ophthalmoscope (cLSO) with approximately a 15-degree field of view to resolve ganglion cells undergoing apoptosis in monkey and rat retinas. This technique has the benefit that the distribution of ganglion cells across the retina can be more readily appreciated than in systems such as the one described in this paper, where the maximum field of view is limited to 3.5 degrees. However, due to the relatively high magnification and reduced impact of higher order aberrations in our instrument, fine structures such as ganglion cell axons can also be resolved. The retrograde labeling method described here is advantageous in situations where it is desirable to image cells repeatedly; we have observed cell labeling for at least five months *in vivo*. This could be useful for retinal disease experiments, for example, imaging the same ganglion cells before, during, and after inducing glaucoma. Additionally, fully functional ganglion cell types could be distinguished *in vivo* by selective dye injections into different regions of the LGN. Combining this with a method to create a lesion to inactivate a cell type, followed by behavioral testing of the living animal, would permit direct analysis of the perceptual role of ganglion cells.

We experimented with the photodynamics of rhodamine dextran dye in our *in vivo* preparation. We observed local brightening of ganglion cell fluorescence due to increased light exposure as shown in Fig. 3. This is the same phenomenon that Dacey et al. [33] observed in an *in vitro* preparation, where ganglion cells were labeled with an LGN injection of the same dye. In Dacey's studies, the increased brightening made dendritic field arbors visible, such that he was able to classify individual cells based on their dendritic morphology. The photodynamic effect provided a means of photo-filling selected ganglion cells where increased light caused the dye to release from the lysosomes in the cell and fill the entire cell,

including its dendrites [33]. Dacey explained the increased brightening phenomenon as reduced self quenching, in which the dye concentration decreases as it spreads throughout the cell and into its dendrites [33]. Combining the high resolution afforded by adaptive optics with the photo-filling properties of rhodamine dextran dye may be a way to image dendritic tree fields, providing a method to classifying ganglion cells morphologically *in vivo* as well as improve the visualization of ganglion cell axons.

4.2 RPE cell imaging *in vivo*

The distribution of lipofuscin autofluorescence across the retina has been well-established, and linked to several retinal diseases [34-38]. To our knowledge, this is the first report of clearly identified individual RPE cells in primate retina *in vivo*. Bindewald et. al. [25] used a cSLO (Heidelberg Retina Angiograph II) to image lipofuscin distribution across a relatively large area of retina. The published images suggest hints of structure, but did not show a complete mosaic. Imanishi et. al. [27] previously used *in vivo* two-photon microscopy to image mouse RPE cells *in vivo* through the sclera. Two-photon microscopy has the capability to image through thick tissue such as the sclera, but also permits functional imaging *in vivo* by spectrally separating the imaging and visible range stimulation wavelengths. This technique has clear advantages over histological studies, and may be improved upon by the use of high-resolution adaptive optics to image through the eye's own optics where the imaging location is not limited to the peripheral retina as it is when imaging through the sclera. The ability to take *in vivo* images of the RPE cell mosaic provides a means to study the morphology of normal and diseased cells as well as their role in retinal diseases and their associated therapies.

4.3 Fluorescein Angiography

The fluorescence AOSLO instrument is not limited to imaging ganglion cells and RPE cells but can take advantage of many fluorescence markers, injected or intrinsic. A simple demonstration of this is high-resolution fluorescein angiography where a completely connected network of the finest capillaries around the foveal avascular zone is visible. We found the full width, half maximum (FWHM) of five capillaries measured around the foveal avascular zone ranged from 5 to 9 μm , possibly slightly increased due to blurring from uncorrected aberrations or low quality reflectance images which yielded a poor dual registration, but are in the range of 3.2 to 7 μm as measured histologically in macaque monkeys by Weinhaus et al. [56]. The fluorescein signal was strong enough to detect in a single frame and the live movie shows blood flow as the dye travels through the small capillaries.

4.4 Benefits and future applications of *in vivo* fluorescence imaging.

The images presented here were obtained during the time in which the adaptive optics system was being developed. These results were obtained in the eye of a young monkey with best-corrected RMS wavefront error of 0.2 to 0.3 μm as measured by our wavefront sensor. A future paper will describe the benefit of adaptive optics in imaging smaller structures than the soma such as ganglion cell dendrites and axons.

Combining confocal detection, and high-resolution adaptive optics *in vivo* imaging creates a confocal fluorescence microscope for the eye, permitting experiments in the living eye that could otherwise only have been conducted in excised tissue. The ability to image a variety of microscopic retinal structures in the living eye may be especially useful in combination with physiological as well as psychophysical measurements. *In vivo* imaging allows changes in normal and diseased retinas to be studied over periods of months to years in a single animal, obviating the need to sacrifice multiple animals at different time points for *in vitro* microscopic analysis. When applied to the study of retinal disease, these methods may allow earlier detection and may facilitate the development of effective therapy. While all the results

shown here are from a monkey, the imaging system was designed to also accommodate humans, rats, and other species. We have successfully imaged RPE cells in humans and the results will be published separately.

5. Conclusion

We have combined confocal detection, fluorescence imaging, adaptive optics, and multi-spectral imaging to obtain high-resolution *in vivo* images of retinal ganglion cells, retinal pigment epithelial cells, and the finest capillaries around the foveal avascular zone in a monkey. These techniques may provide new information about ganglion cell and RPE cell morphology in normal and diseased retinas *in vivo*. When combined with psychophysical testing this technique may also lead to a new understanding of ganglion cell function.

Acknowledgments

This work was supported by a NIH Grant BRP-EY014375, NIH Training Grant-EY07125, NIH Core Grant-EY001319, NSF Grant cfao-ast-9876783 and Grants from Research to Prevent Blindness. We thank Joseph Carroll, Geunyoung Yoon, and Gang Pan, for their contributions and helpful discussions.